Architecture optimization of a parallel Schönflies-motion robot for pick-and-place applications in a predefined workspace

Guanglei Wu [a,b], Shaoping Bai [b,*], Preben Hjørnet [c]

[a] School of Mechanical Engineering, Dalian University of Technology, 116024 Dalian, China
[b] Department of Mechanical and Manufacturing Engineering, Aalborg University, 9220 Aalborg, Denmark
[c] Blue WorkForce A/S, 9900 Frederikshavn, Denmark

ABSTRACT

This paper deals with the architecture optimization of a parallel Schönflies-motion robot admitting a rectangular workspace, which allows to utilize the shop-floor space efficiently for flexible pick-and-place applications. In this work, parametric models including the transmission quality, elasto-statics and dynamics are established and further used in the integrated architectural design optimization. By taking the design requirements and pick-and-place trajectory into consideration, the kinematic and dynamic performances of the robot are optimized with prescribed workspace based on a multi-objective optimization approach. The Pareto-front is obtained, which provides optimal solutions to the robot design. Robot prototyping work based on the optimal results is described.

1. Introduction

Schönflies-motion robots, i.e., robots with three translations and one rotation around the axis of vertical direction, are one class of popular four degree-of-freedom (DOF) pick-and-place (PnP) robots in material handling. The first application of PnP robots in direct food handling was seen in the early 1990s in the bakery industry. This type of serial SCARA robot was able to pick and place at a reasonable rate of 55–80 cycles[1] per minute (cpm), which is too slow to meet the requirement of high-speed operations for high productivity in many industries.

The development of parallel mechanism based robots makes the high-speed PnP operations possible. The Quattro robot [1] by Adept Technologies Inc., shown in Fig. 1(a), which hit the market in 2007, is the fastest industrial robot available. Its latest version can accelerate at more than $15G$ with a 2 kg payload, allowing to accomplish four standard pick-and-place cycles per second. Other parallel PnP robots of three or four limbs [2–8] are also noticeable for their high performance. However, these robots have a cylindrical workspace (WS) due to the fully symmetrical topology architecture, which is not optimal for the PnP operations that are normally confined within a cuboid volume. Besides, there are two-limb parallel Schönflies-motion robots reported in the literature and their WS is of cylindrical shape too [9–11]. In view of the properties of PnP motion, a recently developed robot, namely, the Ragnar robot [12] as shown in Fig. 1(b), was designed with a

_____

* Corresponding author.
  E-mail addresses: gwu@dlut.edu.cn (G. Wu), shb@m-tech.aau.dk (S. Bai), ph@blueworkforce.com (P. Hjørnet).
  [1] A cycle is defined as the movement along a trajectory of 25 × 305 × 25 mm with a 1 kg payload
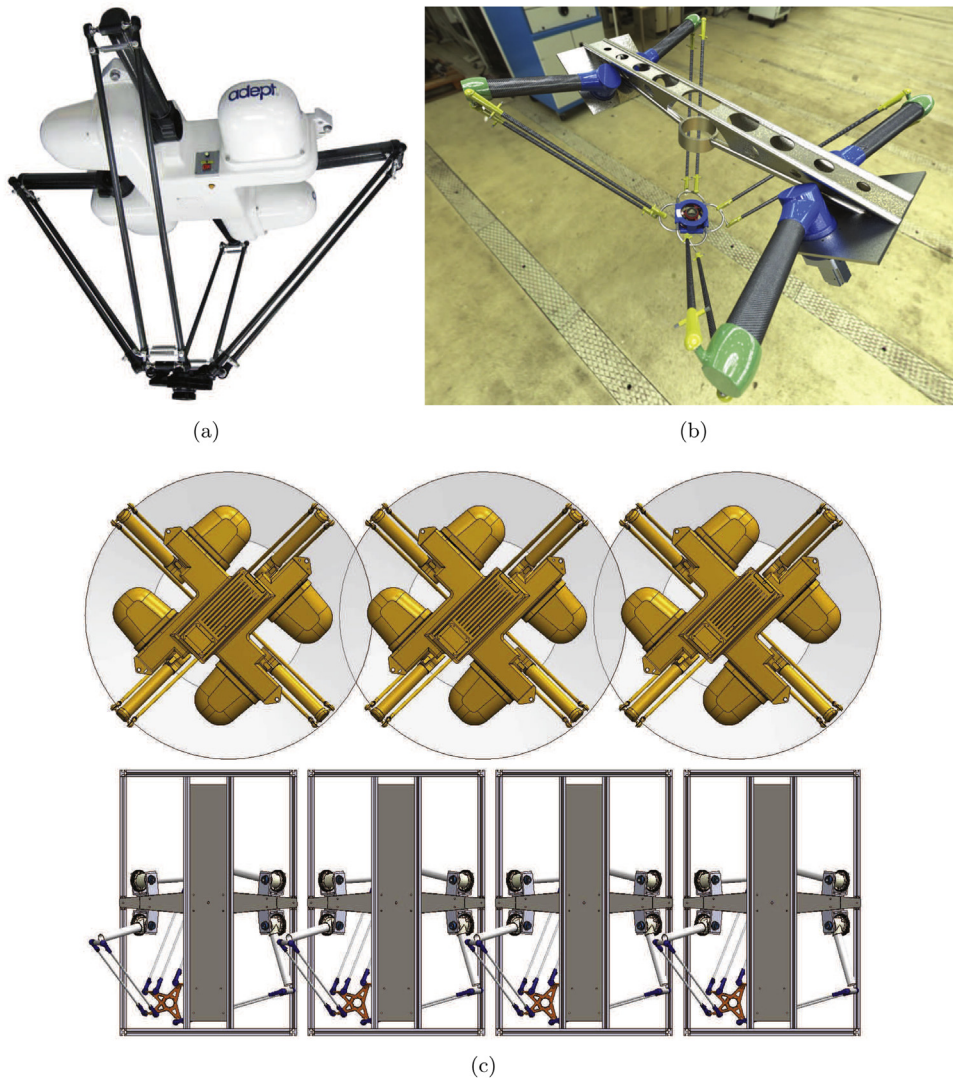
Fig. 1. The parallel Schönflies-motion pick-and-place robots: (a) Quattro [1]; (b) rendered CAD model of Ragnar; and (c) layout of Ragnar robots (bottom), comparing with Quattro robots (top).

rectangular workspace to utilize the shop-floor space more efficiently. By comparing with the layouts of the Quattro robots as displayed in Fig. 1(c), the Ragnar robot, with a rectangular workspace, can be deployed in the production line more compact, allowing more robots to be installed side-by-side in shop-floors for utilization of spaces [13]. In this work, architecture design and optimization are studied to utilize its potential for high performance in a predefined workspace.

2. The state-of-art of architecture design optimization

The design optimization of dedicated pick-and-place robots, like the case of Ragnar, stands for a special type of design problem, in which the robot should be designed for special trajectories (PnP trajectories) in a predefined workspace (rectangular shape), contrary to the design of general-purpose robots. The optimization problem at hand requires not only changes of link dimensions, but also those of architectural parameters, which affects both the workspace shape and robot performance. The optimization problem thus needs new formulations and optimization methods to find the optimum architectural parameters as well as link dimensions.

In the architecture optimization, we take into consideration of both kinematic and kinetostatic/dynamic performances. For the kinematic performance, the characteristics of the workspace that reflects the shape, size and presence of singularities are of primary importance in the PMs design. The workspace optimization of parallel manipulators can usually be solved by means of two different formulations: robot design constrained to a prescribed workspace shape and workspace volume maximization.
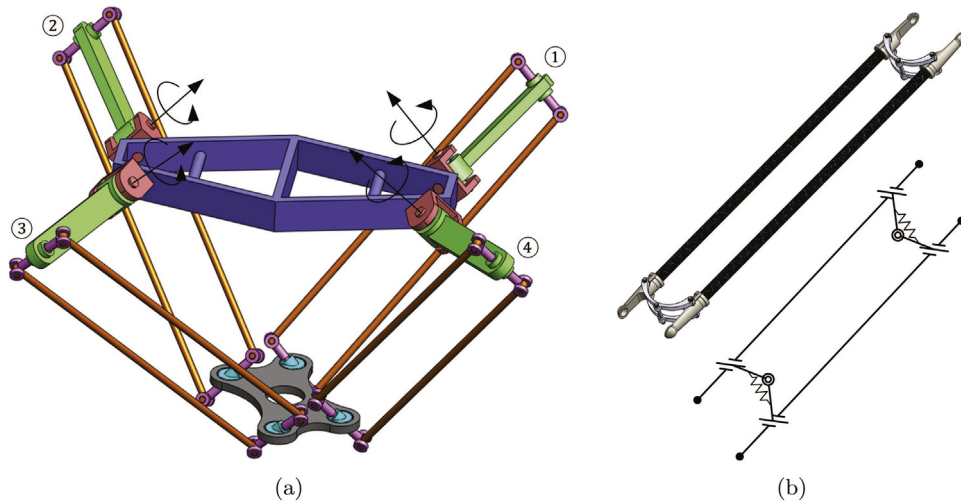
Fig. 2. Schematic of the Ragnar robot: (a) CAD model and (b) a parallelogram.

However, maximizing the manipulator workspace may result in a poor design with regard to the manipulator dexterity/manipulability [14], which is another utmost important concern to map the motion/force [15] between the actuators and end-effector. The dexterity/manipulability is usually evaluated by means of the condition number of the kinematic Jacobian matrix. Altuzarra et al. [16] dealt with the multi-objective optimum design of a linear-actuated parallel Schönflies motion generator, in which the manipulator workspace volume and dexterity were considered as objective functions. In that work, as the Jacobian matrix is not homogeneous, the Jacobian matrix was normalized by a characteristic length to evaluate the dexterity. An efficient approach to accommodate inhomogeneity is to use the concept of the virtual coefficient, namely, the motion/force transmission. Taking the transmission index as performance evaluation, Xie and Liu [8] optimized the kinematic performance of a Quattro-based Schönflies-motion robot, i.e., X4 robot. Besides, Kim et al. [5] reported the kinematic optimal design of a redundant four-limb parallel Schönflies-motion robot with the focus on dexterity.

Compared to kinematic aspects, the kinetostatic/dynamic aspects are more complex as the latter requires a detailed description of the mechanism structure and the evaluation is usually time consuming. Of the kinetostatic aspects, stiffness is particularly important, since it is a measure of the ability of its end-effector to resist deformation due to an external wrench (forces and moments). Moreover, the moment of inertia of the mechanism, input/output torque and energy consumption are important factors to consider. Some works on the kinetostatic/dynamic optimal design of parallel Schönflies-motion robots have also been reported. Taghvaeipour et al. [17] presented the multi-objective optimum design of the McGill SMG [10] aiming to maximize the workspace and stiffness of the robot, whereas the stiffness indices used in this work cannot represent the stiffness behavior naturally. Cammarata and Sinatra [18] illustrated the elastodynamic design optimization with the Schönflies-motion robot introduced by Altuzarra [6]. Based on the commercialized Quattro robot, Pierrot et al. [4] optimized the dynamic performance of the robot with a new articulated mobile platform. Later on, Corbel et al. [19] from the same research group reported that this type of parallel robots can achieve very high acceleration with redundant actuation. Using same structure of the 4-DOF Veloce. robot [7], Liu et al. [20] minimized the maximum singular value of the generalized inertia matrix toward high dynamic characteristics considering the transmission angles in the parallelogram as constraints. In general, the design process simultaneously deals with the kinematic and kinetostatic/dynamic aspects [21], therefore, a systematic design approach considering these criteria as much is preferable. Hernández et al. [22] reported a specification-based design approach, where more concrete and detailed evaluation criteria are needed to be integrated.

In this work, the integrated architecture optimization of the Ragnar robot is presented, based on a multi-objective design optimization approach. Subject to the design specifications, a systematic design optimization concerning the workspace, the transmission quality, the accuracy and the dynamic performance of the mechanism under design is formulated towards high kinematic and kinetostatic/dynamic performances. Moreover, the length of the connecting bar in the parallelogram, which is rarely considered in the previous works, is also considered. The Pareto-front, also called the set of Pareto-optimal solutions, of the multi-objective optimization problem is obtained to offer multiple solutions of optimal design parameters. Robot prototyping work based on the optimal results is described.

3. Robot architectural model

The Ragnar robot displayed in Fig. 2(a) is composed of four identical R̲RΠRR[2]-typed limbs to connect the base and the

---

[2] R and Π stand for revolute joint and parallelogram (Π joint), respectively, and an underlined letter indicates an actuated joint.
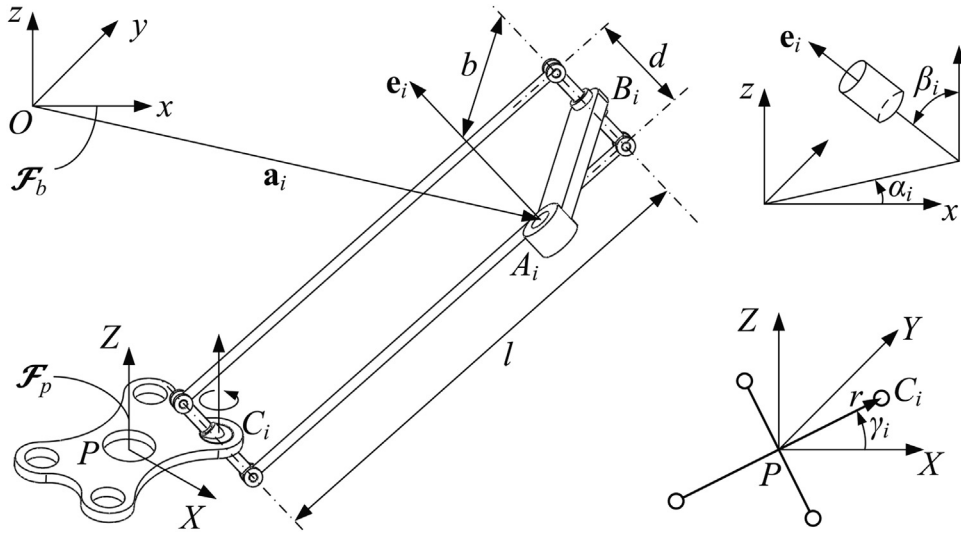
Fig. 3. Parameterization of the ith leg of the Ragnar robot.

mobile platform (MP). In practice, four spherical joints at both ends of the parallelogram are adopted instead of the universal joints to connect the proximal link and MP for rapid prototyping and interchangeability, where the flexure springs are used to keep the Π joint as depicted in Fig. 2(b). Moreover, both proximal and distal links are made of carbon fibre tubes for lightweight design. Different from the Quattro robot, the motors of the Ragnar robot are mounted at different orientations on the base frame, of which the four axes of rotation of the actuated revolute joints are not coplanar. The robot is able to generate the Schönflies motion, as analyzed in Appendix A.

Fig. 3 illustrates the kinematic structure of the ith limb, where the global coordinate frame $\mathcal{F}_b$ is built with the origin located at the geometric center of the base frame, the x-axis being parallel to segment $A_2A_1(A_3A_4)$. The moving coordinate frame $\mathcal{F}_p$ is attached to the mobile platform and the origin is at the geometric center, where the X-axis is parallel to segment $C_2C_1(C_3C_4)$. Here and after, vectors **i**, **j** and **k** represent the unit vectors of x-, y- and z-axis, respectively. The orientation of the ith motor is described by its yaw angle α_i and pitch angle β_i, which means $\mathbf{e}_i = \mathbf{E}_i\mathbf{k}$, $\mathbf{E}_i = \mathbf{R}(z, \alpha_i)\mathbf{R}(y, \beta_i)$, and $-\alpha_{1(3)} = \alpha_{2(4)} = \alpha$, $-\beta_{1(4)} = \beta_{2(3)} = \beta$.

3.1. Design specifications

The Ragnar robot is dedicated to serving in food handling industry, wherein the requirements on speed are high, while the position accuracy is relatively low. The design of Ragnar robot will thus focus on payload, motion region and speed, while the accuracy and robot manipulability will be guaranteed but less important. Similar to the Quattro robot, the payload of the robot in this design is 3 kg and maximum acceleration is $10G$ within the cycle time 0.5 s, or two cycles per second. Moreover, the maximal regular workspace (RWS) is predescribed by a superellipsoid that can contain desired different shaped cuboid volume, which takes the form:

$$\left|\frac{x}{e_x}\right|^n + \left|\frac{y}{e_y}\right|^n + \left|\frac{z}{e_z}\right|^n = 1 \tag{1}$$

Here, n is set to 3 for workspace maximization and rectangular workspace fitting.

By minimizing the kinetic energy, an optimized test trajectory of 25 mm × 305 mm × 25 mm [12] displayed in Fig. 4 is adopted to evaluate the dynamic and elastic performances. The specifications to be achieved by Ragnar robot are summarized in Table 1, where the minimum workspace size ensures the testing PnP trajectory confined within the desired workspace.

3.2. Design variables

As illustrated in Fig. 3, the kinematic and architectural parameters of the robot include a_x, a_y, α, β, b, l, r, γ, d, where d is the length of the connecting bar in the parallelogram rarely considered in the design optimization of this type of parallel robots [16,23,24]. We include this parameter as it influences the stiffness of the robots and finally the deflection at the mobile platform.

In this work, to achieve the optimal design of a series of robots, the length of the proximal link is designated to $b = 300, 350, 400$ mm, respectively. The length of the distal link is then set to $l = \rho b$, with ρ being a ratio greater than 1. The
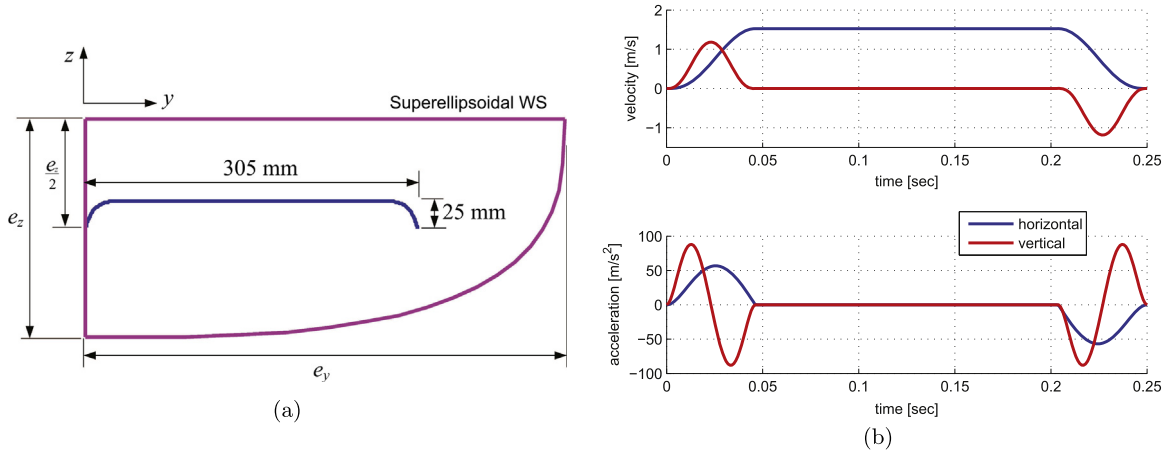
Fig. 4. The pick-and-place trajectory for performance evaluation: (a) trajectory defined in a superellipsoid workspace and (b) velocity/acceleration profiles of half cycle.

Table 1
Design requirements of the Ragnar robot for PnP applications.

Payload (includes end-effector)	3 kg
Minimum WS (mm^3)	$\{e_x, e_y, e_z\}_{min} = \{250, 320, 250\}$
Maximum acceleration	$10G$
Rotation capability	$\phi_{max} = -\phi_{min} = 45°$
Cycle time	0.5 s
Positioning and orientation accuracy	5 mm; 3°

Table 2
The material properties[a] of the proximal and distal links.

Properties	Proximal (∅60/54 mm)	Distal (∅16/14 mm)
ρ_b/ρ_l (g/mm)	1.482	0.075
E (GPa)	110	92
G (GPa)	42.31	35.4

[a] ρ_b and ρ_l stand for material densities of the active link and parallelogram, respectively; E and G stand for Young's and shear moduli, respectively.

structural parameters of the cross-sections of the proximal and distal arms are fixed for modular design and interchangeability. The corresponding material and mass properties of the mobile bodies are given in Tables 2 and 3, respectively. Moreover, the motor pitch angle β is set to 45° for the reachable workspace free of collision, thus, the design variables of the architecture optimization problem at hand are defined as:

$$\mathbf{x} = \begin{bmatrix} a_x & a_y & \alpha & \rho & r & \gamma & d \end{bmatrix} \tag{2}$$

where a_x, a_y, α, r, γ are architectural parameters of the robot, and ρ, d are link length parameters.

4. Kinematic, kinetostatic and dynamic modeling of Ragnar robot

Under the coordinate systems of Fig. 3, the position vectors of point A_i in frame $\mathcal{F}_b$ are denoted by

$$\mathbf{a}_1 = -\mathbf{a}_3 = \begin{bmatrix} a_x & a_y & 0 \end{bmatrix}^T; \quad \mathbf{a}_2 = -\mathbf{a}_4 = \begin{bmatrix} -a_x & a_y & 0 \end{bmatrix}^T \tag{3}$$

The position vector of point B_i is derived as

$$\mathbf{b}_i = b\mathbf{h}_i + \mathbf{a}_i; \quad \mathbf{h}_i = \mathbf{R}_i \mathbf{i}, \quad i = 1, ..., 4 \tag{4}$$

where $\mathbf{R}_i = \mathbf{E}_i \mathbf{R}(z, \theta_i)$, and θ_i is the angle of rotation of motor from a reference position.

Let the mobile platform pose be denoted by $\chi = \begin{bmatrix} \mathbf{p}^T & \phi \end{bmatrix}^T$, $\mathbf{p} = \begin{bmatrix} x & y & z \end{bmatrix}^T$, the Cartesian coordinates of point C_i are expressed

Table 3
Parametric mass properties for dynamic evaluation.

Mass of active link	m_b (kg)	$1.5 + \rho_b(b - 30)$
Moment of inertia of active link around $\mathbf{e}_i$	I_b (kg mm^2)	$m_b b^2/3$
Mass of parallelogram	m_l (kg)	$0.325 + 2\rho_l(l - 40)$
Mass of connecting bar on the mobile platform	m_j (kg)	0.2
Mass of mobile platform	m_p (kg)	3
Moment of inertia of mobile platform	I_p (kg mm^2)	$m_p r^2/3$

as

$$\mathbf{c}_i = \mathbf{Q}\mathbf{c}'_i + \mathbf{p} \tag{5}$$

where $\mathbf{Q} = \mathbf{R}(z, \phi)$ is the rotation matrix of the MP and $\mathbf{c}'_i$ is the position vector of C_i in the frame $\mathcal{F}_p$:

$$\mathbf{c}'_i = r\left[\cos\gamma_i \quad \sin\gamma_i \quad 0\right]^T; \quad \gamma_1 = -\gamma_4 = \gamma, \gamma_{2(3)} = \pi \mp \gamma \tag{6}$$

4.1. Inverse geometry and Jacobian matrices

The inverse geometric problem is solved from the following loop-closure equation:

$$\|\mathbf{c}_i - \mathbf{b}_i\|^2 = l^2, \quad i = 1, ..., 4 \tag{7}$$

To this end, the inverse geometric problem of this robot is solved as

$$\theta_i = 2\tan^{-1}\frac{-I_i \pm \sqrt{I_i^2 + J_i^2 - K_i^2}}{K_i - J_i} \tag{8}$$

with

$$I_i = 2b\mathbf{m}_i^T\mathbf{E}_i\mathbf{j}; \quad J_i = 2b\mathbf{m}_i^T\mathbf{E}_i\mathbf{i}; \quad K_i = \|\mathbf{m}_i\|^2 + b^2 - l^2 \tag{9}$$

where $\mathbf{m}_i = \mathbf{a}_i - \mathbf{c}_i$.

From Eq. (8), it is seen that each limb has two solutions corresponding to two working modes, which is characterized by the sign "$- / +$" in the equation. Here, the "$- + - +$" mode is selected as the working mode. The forward geometric problem was described in Ref. [6].

Differentiating the four equations in (7) with respect to time leads to

$$\mathbf{A}\dot{\chi} = \mathbf{B}\dot{\theta} \tag{10}$$

with

$$\mathbf{A} = \left[\mathbf{j}_1 \quad \mathbf{j}_2 \quad \mathbf{j}_3 \quad \mathbf{j}_4\right]^T; \quad \dot{\chi} = \left[\dot{x} \quad \dot{y} \quad \dot{z} \quad \dot{\phi}\right]^T \tag{11a}$$

$$\mathbf{B} = \text{diag}\left[h_1 \quad h_2 \quad h_3 \quad h_4\right]; \quad \dot{\theta} = \left[\dot{\theta}_1 \quad \dot{\theta}_2 \quad \dot{\theta}_3 \quad \dot{\theta}_4\right]^T \tag{11b}$$

where $\mathbf{A}$ and $\mathbf{B}$ are the forward and inverse Jacobians, respectively, and

$$\mathbf{j}_i = \left[(\mathbf{c}_i - \mathbf{b}_i)^T \quad (\mathbf{k} \times (\mathbf{c}_i - \mathbf{p}))^T \quad (\mathbf{c}_i - \mathbf{b}_i)\right]^T \tag{12a}$$

$$h_i = (\mathbf{e}_i \times (\mathbf{b}_i - \mathbf{a}_i))^T(\mathbf{c}_i - \mathbf{b}_i) \tag{12b}$$

The kinematic Jacobian matrix is obtained as

$$\mathbf{J} = \mathbf{A}^{-1}\mathbf{B} \tag{13}$$

4.2. Transmission index

A manipulator has to transmit motion/force between the input and the output links, hence, transmission index (TI) is of importance to be defined to evaluate the transmission performance of the manipulator. This will be done with the transmission performance at both the input and output of the manipulator.
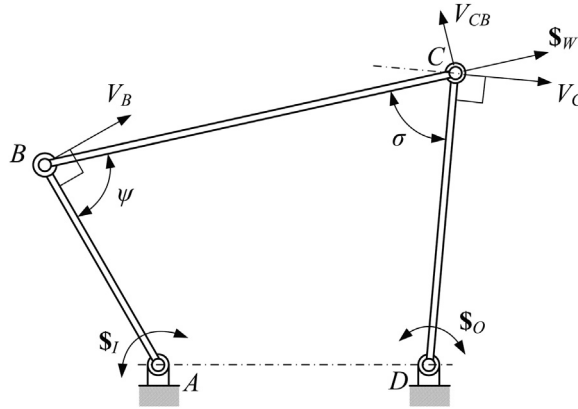
Fig. 5. Transmission wrench and twist screw of a planar four-bar linkage.

4.2.1. Input transmission index

In a robot linkage, the motion is transmitted from the input link to the output one. The internal wrench arising due to the transmission is called the transmission wrench, which can be expressed by the transmission wrench screw (TWS). In order to evaluate the input transmission performance, the power coefficient between the TWS and the input twist screw is defined as its input transmission index. For the Ragnar robot, each leg has one active revolute joint, thus, the unit input twist screw of the ith limb is expressed as

$$\hat{\$}_{Ii} = \begin{bmatrix} \mathbf{e}_i \\ \mathbf{0}_3 \end{bmatrix}; \quad i = 1, ..., 4 \tag{14}$$

and the TWS of the ith limb, a pure force along the link B_iC_i, is defined as

$$\hat{\$}_{Ti} = \begin{bmatrix} \mathbf{s}_i \\ (\mathbf{b}_i - \mathbf{a}_i) \times \mathbf{s}_i \end{bmatrix} \tag{15}$$

where $\mathbf{s}_i$ is the unit vector parallel to the distal link of ith limb, which is defined as

$$\mathbf{s}_i = \frac{\mathbf{c}_i - \mathbf{b}_i}{\| \mathbf{c}_i - \mathbf{b}_i \|} \tag{16}$$

The transmission index of the ith limb can be defined as [25]

$$\lambda_i = \frac{|\hat{\$}_{Ii} \circ \hat{\$}_{Ti}|}{|\hat{\$}_{Ii} \circ \hat{\$}_{Ti}|_{\max}} \tag{17}$$

This index corresponds to a function of the transmission angle, which is the smallest angle between the direction of velocity of the driven link and the direction of absolute velocity vector of output link both taken at the common point [26]. For instance as the four-bar linkage illustrated in Fig. 5, it is the angle ψ between the driving link and the coupler, also known as inverse transmission angle [27], therefore, the input transmission index can be expressed as $\lambda = | \sin \psi|$.

4.2.2. Output transmission index

As the robot produces Schönflies motion, the instantaneous motion of the mobile platform, i.e., the output twist, will be three translations and one rotation about the vertical axis, for which the unit output twist screw (OTS) of the ith limb takes the following form:

$$\hat{\$}_{Oi} = \begin{bmatrix} \mathbf{k} \\ \zeta_i \end{bmatrix}; \quad i = 1, ..., 4 \tag{18}$$

where the vector ζ_i can be calculated from [28]

$$\hat{\$}_{Oi} \circ \hat{\$}_{Tj} = 0; \quad i, j \in \{1, 2, 3, 4\}, \quad i \neq j \tag{19}$$

Similarly, the transmission index of the i th limb is defined as

$$\eta_i = \frac{|\hat{\$}_{Oi} \circ \hat{\$}_{Ti}|}{|\hat{\$}_{Oi} \circ \hat{\$}_{Ti}|_{\max}} \tag{20}$$

Likewise, this index is associated with the forward transmission angle σ in Fig. 5, the output transmission index being denoted by $\eta = |\sin \sigma|$.

4.2.3. Local and global transmission index

Based on the two indices defined, the local transmission index (LTI) [28] of the manipulator, namely, the transmission index in a prescribed configuration, is defined as:

$$\mu = \min\{\lambda_i \cdot \eta_i\}; \quad i \in \{1, 2, 3, 4\} \tag{21}$$

The higher the value μ, the higher the quality of input and output transmission. The distribution of the LTI can indicate the workspace (WS) region of better transmissibility. Thus, this index can be used for either the evaluation of the transmission or the design optimization.

To evaluate the transmissibility of the manipulator within a prescribed workspace Ω, a global transmission index (GTI) is defined over the workspace Ω, which is calculated through a discrete approach in practice, namely,

$$\text{GTI} = \frac{\int \mu \, d\Omega}{\int d\Omega} \quad \text{or} \quad \text{GTI} = \frac{1}{\Omega} \sum_{i=1}^{n} \mu_i \Delta \Omega = \frac{1}{n} \sum_{i=1}^{n} \mu_i \tag{22}$$

where n is the discrete number of workspace points. The index obtained through the above equation is an arithmetic mean, which can be replaced with a quadratic mean for a better indication of the transmission [29], subsequently, GTI is redefined as

$$\text{GTI} = \sqrt{\frac{1}{n} \sum_{i=1}^{n} \mu_i^2} \tag{23}$$

The higher the GTI, the better the robot transmission quality.

4.3. Cartesian stiffness matrix

A commonly used approach to model the stiffness matrix of the parallel robots is the Virtual Joint Method (VJM) [30–34], as it provides acceptable accuracy in short computational time. Here, the Cartesian stiffness matrix is computed with the virtual-spring approach [34,35] based on screw theory [36], where the mobile platform can be considered as rigid compared to the kinematic linkages since it will be manufactured as a solid block. The Jacobian matrices corresponding to the deflections and variations at passive joints in the i th limb are found as below:

$$\mathbf{J}_{\theta i} = \left[\hat{\$}_{\theta}^{i} \; \hat{\$}_{b1}^{i} \; \dots \; \hat{\$}_{b6}^{i} \; \hat{\$}_{c1}^{i} \; \dots \; \hat{\$}_{c5}^{i} \right] \in \mathbb{R}^{6 \times 12} \tag{24a}$$

$$\mathbf{J}_{qi} = \left[\hat{\$}_{b3}^{i} \; \hat{\$}_{q1}^{i} \; \hat{\$}_{q2}^{i} \right] \in \mathbb{R}^{6 \times 3} \tag{24b}$$

where the unit screws are expressed as

$$
\hat{\$}_{\theta}^{i} = \begin{bmatrix} \mathbf{e}_i \\ \mathbf{r}_{ai} \times \mathbf{e}_i \end{bmatrix}; \quad \hat{\$}_{q1}^{i} = \begin{bmatrix} \mathbf{e}_i \\ \mathbf{r}_{ci} \times \mathbf{e}_i \end{bmatrix}; \quad \hat{\$}_{q2}^{i} = \begin{bmatrix} \mathbf{k} \\ \mathbf{r}_{ci} \times \mathbf{k} \end{bmatrix}
$$
$$
\hat{\$}_{b1}^{i} = \begin{bmatrix} \mathbf{h}_i \\ \mathbf{r}_{bi} \times \mathbf{h}_i \end{bmatrix}; \quad \hat{\$}_{b2}^{i} = \begin{bmatrix} \mathbf{t}_i \\ \mathbf{r}_{bi} \times \mathbf{t}_i \end{bmatrix}; \quad \hat{\$}_{b3}^{i} = \begin{bmatrix} \mathbf{e}_i \\ \mathbf{r}_{bi} \times \mathbf{e}_i \end{bmatrix}; \quad \hat{\$}_{b4}^{i} = \begin{bmatrix} \mathbf{0}_3 \\ \mathbf{h}_i \end{bmatrix}; \quad \hat{\$}_{b5}^{i} = \begin{bmatrix} \mathbf{0}_3 \\ \mathbf{e}_i \end{bmatrix}; \quad \hat{\$}_{b6}^{i} = \begin{bmatrix} \mathbf{0}_3 \\ \mathbf{t}_i \end{bmatrix}
$$
$$
\hat{\$}_{c1}^{i} = \begin{bmatrix} \mathbf{s}_i \\ \mathbf{r}_{ci} \times \mathbf{s}_i \end{bmatrix}; \quad \hat{\$}_{c2}^{i} = \begin{bmatrix} \mathbf{u}_i \\ \mathbf{r}_{ci} \times \mathbf{u}_i \end{bmatrix}; \quad \hat{\$}_{c3}^{i} = \begin{bmatrix} \mathbf{v}_i \\ \mathbf{r}_{ci} \times \mathbf{v}_i \end{bmatrix}; \quad \hat{\$}_{c4}^{i} = \begin{bmatrix} \mathbf{0}_3 \\ \mathbf{s}_i \end{bmatrix}; \quad \hat{\$}_{c5}^{i} = \begin{bmatrix} \mathbf{0}_3 \\ \mathbf{u}_i \end{bmatrix} \tag{25}
$$

where

$$\mathbf{r}_{ai} = \mathbf{a}_i - \mathbf{p}; \quad \mathbf{r}_{bi} = \mathbf{b}_i - \mathbf{p}; \quad \mathbf{r}_{ci} = \mathbf{c}_i - \mathbf{p}; \quad \mathbf{t}_i = \mathbf{R}_i \mathbf{j}; \quad \mathbf{u}_i = \frac{\mathbf{s}_i \times \mathbf{e}_i}{\| \mathbf{s}_i \times \mathbf{e}_i \|}; \quad \mathbf{v}_i = \frac{\mathbf{s}_i \times \mathbf{u}_i}{\| \mathbf{s}_i \times \mathbf{u}_i \|} \tag{26}$$

Moreover, the stiffness matrix in the joint space is

$$\mathbf{K}_{\theta i} = \text{diag}\left[K_{\text{act},i} \; \mathbf{K}_b \; \mathbf{K}_{\Pi} \right] \in \mathbb{R}^{12} \tag{27}$$

where $K_{\text{act},i}$ stands for the stiffness of the i th actuator and $\mathbf{K}_{\Pi}$ is the stiffness matrix of the parallelogram link given in Appendix B. Matrix $\mathbf{K}_b$ denotes the stiffness matrix of a proximal arm modeled by a cantilever, i.e., $\mathbf{K}_b = [k_{ij}]$, the non-zero elements being expressed as:

$$k_{11} = \frac{GI_x}{L}; \quad k_{22} = \frac{4EI_y}{L}; \quad k_{33} = \frac{4EI_z}{L}; \quad k_{44} = \frac{EA}{L}; \quad k_{55} = \frac{12EI_z}{L^3}; \quad k_{66} = \frac{12EI_y}{L^3} k_{26} = k_{62} = \frac{6EI_y}{L^2}; \quad k_{35} = k_{53} = -\frac{6EI_z}{L^2} \tag{28}$$

where L is the link length, A is its cross-section area, I_y, I_z, and I_x are the quadratic and polar moments of inertia of the cross-section, and E and G are Young's and shear moduli, respectively.

The Cartesian stiffness matrix $\mathbf{K}_i$ of the i th leg is the first six dimensional entry extracted from the following matrix:

$$\mathbf{K}'_i = \begin{bmatrix} \mathbf{J}_{\theta i} \mathbf{K}_{\theta i}^{-1} \mathbf{J}_{\theta i}^T & \mathbf{J}_{qi} \\ \mathbf{J}_{qi}^T & \mathbf{0}_3 \end{bmatrix}^{-1} \tag{29}$$

As a result, the Cartesian stiffness matrix is the summation of the stiffness matrices of the four limbs, namely,

$$\mathbf{K} = \sum_{i=1}^{4} \mathbf{K}_i \tag{30}$$

4.4. Dynamic modeling

The actuator torques and powers can be solved by using the Lagrange equations [37]

$$\frac{\mathrm{d}}{\mathrm{d}t}\left(\frac{\partial L}{\partial \dot{\mathbf{q}}}\right) - \frac{\partial L}{\partial \mathbf{q}} + \mathbf{C}_q^T \lambda = \mathbf{Q}_{ex} \tag{31}$$

where $L \equiv T - V$ is the Lagrangian of the system, including the mobile platform and the four legs, and $\mathbf{q} = \begin{bmatrix} \theta^T \chi^T \end{bmatrix}^T$, $\theta = \begin{bmatrix} \theta_1, \theta_2, \theta_3, \theta_4 \end{bmatrix}^T$. Moreover, $\mathbf{Q}_{ex} = [\tau^T, \mathbf{0}]^T \in \mathbb{R}^8$ is the vector of external forces and vector $\tau = [\tau_1, \tau_2, \tau_3, \tau_4]^T$ characterizes the actuator torques. Matrix $\mathbf{C}_q = \begin{bmatrix} \mathbf{B} & -\mathbf{A} \end{bmatrix}$ is the system's constraint Jacobian. Moreover, $\lambda = \begin{bmatrix} \lambda_1, \lambda_2, \lambda_3, \lambda_4 \end{bmatrix}^T$ is a vector of Lagrange multipliers.

In this modeling, the influence of the rotation of the distal link can be ignored which is not considered for simplification [12], thus, the kinetic and potential energies are calculated below:

$$T = \frac{1}{2}\left[\sum_{i=1}^{4}\left(I_b \dot{\theta}_i^2 + \frac{1}{4}m_l \parallel \dot{\mathbf{b}}_i + \dot{\mathbf{c}}_i \parallel^2 + m_j \dot{\mathbf{c}}_i^T \dot{\mathbf{c}}_i \right) + \dot{\mathbf{x}}^T \mathbf{M}_p \dot{\mathbf{x}} \right] \tag{32a}$$

$$V = \sum_{i=1}^{4}\left[\frac{1}{2}m_b \mathbf{b}_i + \frac{1}{2}m_l(\mathbf{b}_i + \mathbf{c}_i) + m_j \mathbf{c}_i \right] \cdot \mathbf{g} + m_p \mathbf{p} \cdot \mathbf{g} \tag{32b}$$

where I_b and m_b are the moment of inertia and mass of the proximal arm, respectively, and m_l, m_p and m_j are the masses of the distal arm, mobile platform and the joint on the latter, respectively. Moreover, $\mathbf{M}_p = \mathrm{diag}\begin{bmatrix} m_p & m_p & m_p & I_p \end{bmatrix}$ is the mass matrix of the mobile platform. Terms $\dot{\mathbf{b}}_i$ and $\dot{\mathbf{c}}_i$ stand for the velocities of points B_i and C_i, respectively, which can be calculated with known $\dot{\theta}_i$ and $\dot{\mathbf{x}}$. Additionally, $\mathbf{g} = [0, 0, -9.806]^T$. In the above formulation, it is assumed that the centers of mass of the distal arms are coincident to their geometric centers.

Substituting Eqs. (32a) and (32b) into Eq. (31), all the terms in the equation of motion for this system can be derived. With payload $\mathbf{f}$, the actuator torques are expressed as:

$$\tau_a = \tau - \mathbf{J}^T \mathbf{f} \tag{33}$$

5. Formulation of design optimization

The design criteria are usually antagonistic, for which an efficient approach to handle the design problem is to treat the design optimization as a multi-objective optimization problem, which takes multiple evaluation criteria into account. Henceforth, the architecture optimization of the Ragnar robot will be based on the multi-objective design optimization approach.

5.1. Objective functions

In order for the robot to be adaptive for different installation circumstances, the first objective function in this problem is to maximize the volume of the superellipsoid:

$$f_1(\mathbf{x}) = V_\Omega = 4e_x e_y e_z \frac{\Gamma\left(1 + n^{-1}\right)^3}{\Gamma\left(1 + 3n^{-1}\right)} \quad \rightarrow \quad \max \tag{34}$$

where Γ stands for the Gamma function to compute the volume of a superellipsoid [38].
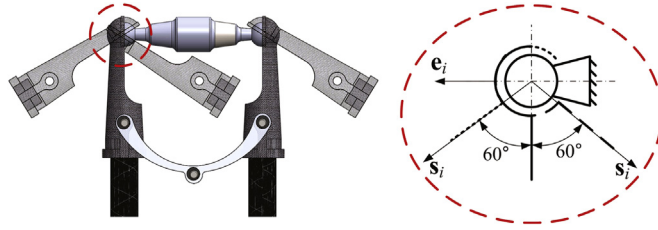
Fig. 6. The motion ranges of the spherical joint in the parallelogram.

Aiming to obtain a better manipulability, the second objective is to maximize the GTI, namely,

$$f_2(\mathbf{x}) = \mathrm{GTI} \quad \rightarrow \quad \mathrm{max} \tag{35}$$

Another important consideration is to minimize the driving torques for the PnP motion along the trajectory as shown in Fig. 4. The third objective is to minimize the maximum values of the root-mean-squared torque T_{rms}^i, $i = 1, \ldots, 4$, namely,

$$f_3(\mathbf{x}) = T_{\mathrm{max}} = \mathrm{max}(T_{rms}^i) \quad \rightarrow \quad \mathrm{min} \tag{36}$$

5.2. Optimization constraints

The other design criteria, such as the kinematic constraints and elastic performance of the manipulator, are considered as constraints, wherein the constraints on the link strength are to guarantee the positioning accuracy.

5.2.1. Geometric constraints

From $l = \rho b$, the ratio of the link lengths of the proximal and distal arms is subject to the following inequality:

$$1.8 \leq \rho \leq 2.2 \tag{37}$$

which is defined for the purpose of convergence of optimization according to the existing designs, such as Delta and Quattro robots.

In addition, the spherical joints in the parallelogram have limited motion ranges, as displayed in Fig. 6, therefore, the reachable workspace of the robot is subject to the following constraint on the spherical joint:

$$30° \leq q_i \leq 150° \tag{38}$$

where $q_i = \cos^{-1}(\mathbf{e}_i \cdot \mathbf{s}_i)$, $i = 1, \ldots, 4$.

5.2.2. Accuracy constraints

The accuracy constraints of the optimization problem are related to the maximum positioning and orientation deflections of the moving-platform subject to a given wrench applied on the latter, thus, the accuracy constraints can be written as:

$$\| \Delta\mathbf{p} \| \leq \epsilon_p; \quad \| \Delta\boldsymbol{\phi} \| \leq \epsilon_\phi \tag{39}$$

where $\Delta\mathbf{p}$ and $\Delta\boldsymbol{\phi}$, calculated from $\left[\Delta\boldsymbol{\phi}^T \ \Delta\mathbf{p}^T \right]^T = \mathbf{K}^{-1}\mathbf{f}$, are the positioning and orientation errors, respectively, and $\mathbf{f}$ is the vector of wrench including the inertia and gravity forces. Moreover, ϵ_p and ϵ_ϕ are the acceptable tolerances of positioning and orientation errors, respectively.

5.3. Multi-objective design optimization problem

Mathematically, the multi-objective design optimization problem is formulated as:

Table 4
Algorithm parameters of the implemented NSGA-II.

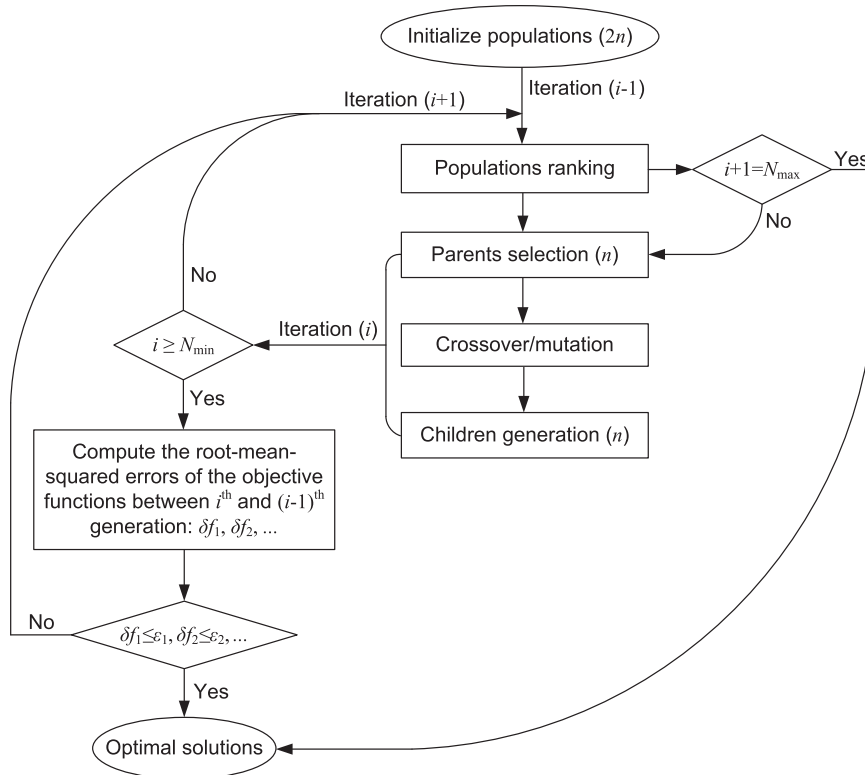|	
Population size	30
Max-/minimum number of generation N_{max}/N_{min}	1000/200
Directional crossover probability	0.5
Crossover probability	0.85
Distribution index	20

Fig. 7. The flow chart of the GA multi-objective optimization procedure.

$$\text{maximize} \quad f_1(\mathbf{x}) = V_\Omega$$
$$\text{maximize} \quad f_2(\mathbf{x}) = \text{GTI}$$
$$\text{minimize} \quad f_3(\mathbf{x}) = T_{max}$$
$$\text{over} \quad \mathbf{x} = \begin{bmatrix} a_x & a_y & \alpha & \rho & r & \gamma & d \end{bmatrix}$$
$$\text{subject to} \quad g_1: 1.8 \le \rho \le 2.2$$
$$g_2: 30° \le q_i \le 150°$$
$$g_3: \phi_{min} \le \phi \le \phi_{max}$$
$$g_4: a \ge a_{min}, \quad b \ge b_{min}, \quad c \ge c_{min}$$
$$g_5: \| \Delta\mathbf{p} \| \le \epsilon_p; \quad \| \Delta\boldsymbol{\phi} \| \le \epsilon_\phi \tag{40}$$

6. Optimal results and discussion

The multi-objective design optimization problem (40) was solved by the non-dominated sorting genetic algorithm (NSGA-II) [39] implemented in *MATLAB*, for which the algorithm parameters are given in Table 4. As GA multi-objective optimization is a stochastic, time-demanding procedure, after the evolutions of a minimum number of iteration N_{min}, the root-mean-squared errors between the objective function values of the current iteration and those of the previous one are

Table 5
Upper and lower bounds of the design variables.

Variables $\mathbf{x}$	$\mathbf{x}_{lb}$	$\mathbf{x}_{ub}$
a_x (mm)	250(250/300)	300(350/400)
a_y (mm)	70	150
α (deg)	15	30
r (mm)	70(80/100)	130(150)
γ (deg)	30	60
d (mm)	70(80)	100(120)
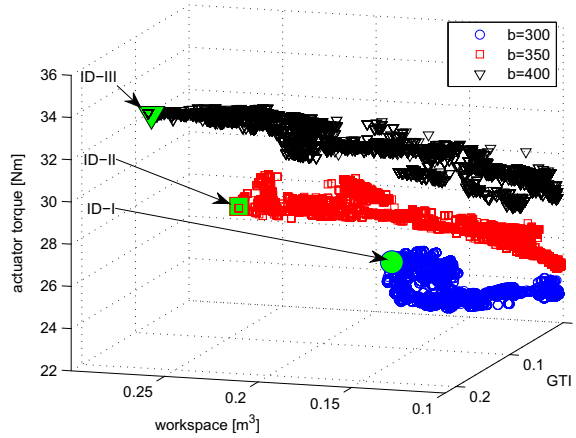
Fig. 8. The Pareto-front of the multi-objective optimization problem.

Table 6
Three optimal solutions of the Pareto-front.

Solution no.	Design variables								Objective values			Constraint values	
	a_x (mm)	a_y (mm)	α (deg)	b (mm)	l (mm)	r (mm)	γ (deg)	d (mm)	V_Ω (mm^3)	GTI	T_{rms} (N m)	$\parallel \Delta\mathbf{p} \parallel$ (mm)	$\parallel \Delta\boldsymbol{\phi} \parallel$ (deg)
ID-I	300	70	15	300	660	70	60	77	0.16	0.12	26.36	4.69	1.18
ID-II	343	84	15	350	756	80	45	108	0.24	0.13	28.73	4.90	2.47
ID-III	380	72	15	400	753	100	45	108	0.29	0.11	32.51	4.91	2.24

calculated and compared for rapid convergence. If the relative computation errors are smaller than the acceptable tolerances, the objectives of the current iteration can be considered as convergent and the corresponding variables are selected as the optimal solutions. Otherwise, the evolution will continue till the maximum iteration $N_{\max}$. The corresponding evolutionary procedure is illustrated in Fig. 7.

The lower and upper bounds of the design variables, denoted by $\mathbf{x}_{lb}$ and $\mathbf{x}_{ub}$, are listed in Table 5, where the ranges of a_x/a_y, r/γ and d are designated with the consideration of free of collision and compactness. Moreover, α is set to positive to avoid singularity and its upper bound is to guarantee the rectangular workspace. The upper link length b takes values of 300, 350 and 400 mm, corresponding to three design series of the robot.

6.1. Pareto-optimal solutions

The Pareto-front of the optimization problem was obtained, as shown in Fig. 8. Three Pareto-optimal solutions named ID-I, ID-II, and ID-III on the Pareto-front, as listed in Table 6, are selected as the optimal designs for the robot series of $b = 300$, 350, and 400, respectively. From Table 6, it is seen that the yaw angle of the motor converges to 15° for all the three sets of parameters. Larger x coordinate a_x and smaller y coordinate a_y of the motor positions and larger angle γ of the mobile platform can make the robot have better performances. Moreover, the radius r of the mobile platform converges to its lower bound, and the length d of the connecting bar in the parallelogram increases with the increasing link dimensions of the robot. In addition, Fig. 9 illustrates the box plot of the 30 groups of the objective values of the final generation, which shows
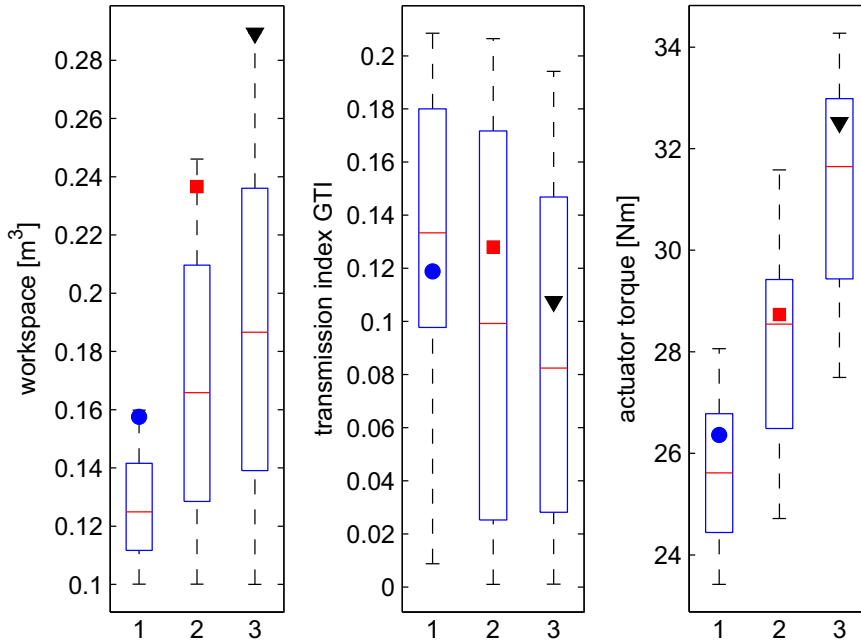
Fig. 9. Boxplot of optimal objectives. Nos. 1, 2 and 3 of horizontal axes stand for the cases of $b = 300, 350, 400$, respectively.

that the two objectives of transmission and actuator torque of the three designs approximate to the mean values of the 30 populations when the workspace reach to the maximum. This means that the designs ID-I, II and III are relatively better design candidates, since the three objectives are antagonistic.

The approximate regular workspace and isocontours of the minimum local transmission index of the three designs are visualized in Fig. 10, respectively. In view of the LTI distributions and the GTI in Table 6, the larger the robot linkage dimensions, the larger the differences between the maximum and minimum local transmission indices. On the top cross-section of the cuboid workspace, the manipulability performance increases with the increasing y coordinates, which is opposite to the varying of the manipulability on the bottom.

Fig. 11 depicts the dynamic simulation results of ID-I and ID-III along the trajectory in Fig. 4, respectively, where a gear box with a reduction ratio of 30 is selected and used for each motor. It is observed that these two designs have very close requirements on the actuators due to the lightweight design although they have significantly different geometric dimensions. It is noteworthy that the elastic deformations are much larger at the beginning of the trajectory than those at the end, which means that the stiffness of the robot increases with the increasing y coordinates. This is consistent with the results in Fig. 14.

6.2. Evaluation with the predefined trajectory

The performances of the robot are also evaluated along different trajectories within the cuboid workspace as shown in Fig. 12. In total, seven trajectories are considered. They include four PnP trajectories (T0 and T3–6) defined along the y-axis with different locations and two circular paths (T1–2) on the top and bottom cross-sections of the cuboid workspace, which are expressed as

$$x = 300 \cos(4\pi t), \quad y = 300 \sin(4\pi t), \quad z = \begin{cases} -510, & \text{T1} \\ -770, & \text{T2} \end{cases}; \quad t \in [0, 0.5] \text{ s} \tag{41}$$

By comparison of the maximum actuator torques/powers and elastic deformations listed in Table 7 and Fig. 13, the "worst" cases exist on the two trajectories in the color of black on the boundaries, where the PnP operation rarely takes place, and the corresponding results are displayed in Fig. 14. In view of the results in Fig. 11(b) and Fig. 14, the trajectory in Fig. 4, which is included in the region of frequent PnP operations, can be used to evaluate the kinetostatic/dynamic performances of the robot in the optimization.

6.3. Robot prototype

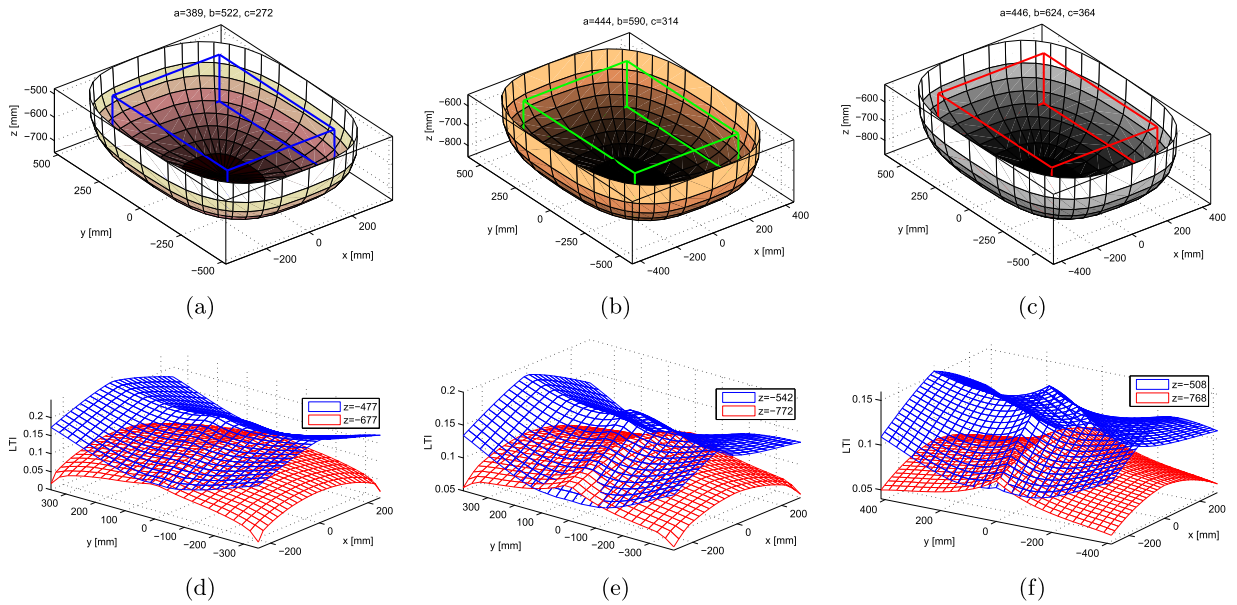Fig. 15 shows a prototype of the Ragnar robot with link length $b = 300$ mm. A few parts, including the mobile platform,

Fig. 10. The approximate regular workspace and isocontours of the minimum local transmission index μ throughout the cuboid workspace: (a, d) ID-I; (b, e) ID-II; and (c, f) ID-III.
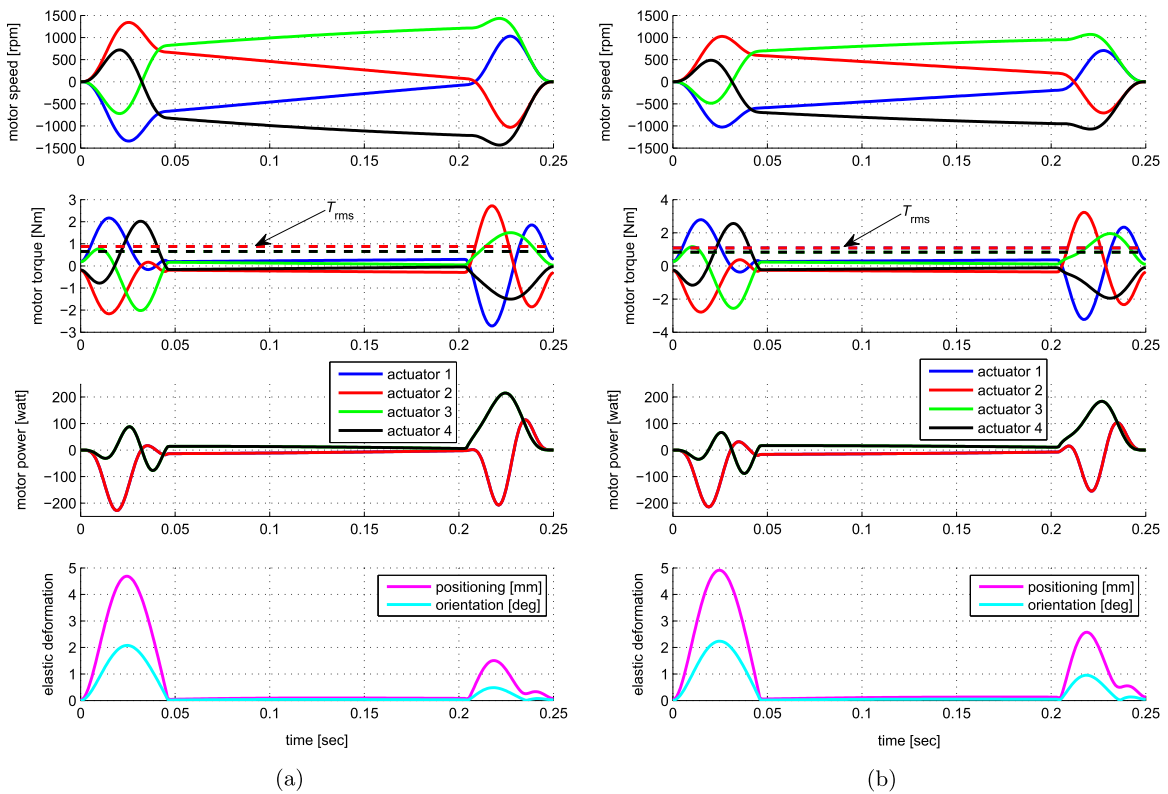

Fig. 11. Comparison of two designs in terms of motor speed, torque, power and end-effector deflections (from top to bottom) : (a) ID-I and (b) ID-III.

studs of spherical joints and plastic springs for the parallelogram, were made by 3D printing. The actuation of the Ragnar robot combines Bosch Rexroth motors and Harmonic Drives. The Robot Operating System (ROS) is adopted for building the control system.
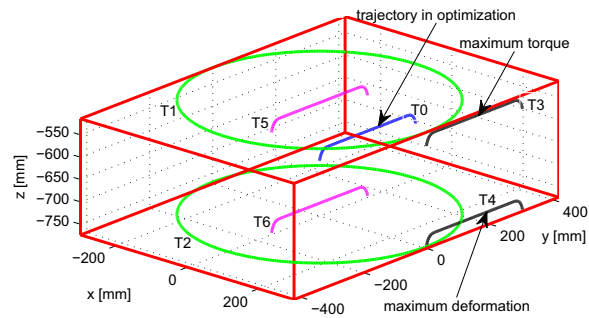
Fig. 12. Testing trajectories within the cuboid workspace of design ID-III.

Table 7
Comparison of performances with the seven trajectories.

Trajectory	T_{max} (N m)	Power (W)	Speed (rpm)	$\| \delta \mathbf{p} \|$ (mm)	$\| \delta \boldsymbol{\phi} \|$ (deg)
T0	1.084	184	1072	4.914	2.238
T1	1.913	408	2288	2.900	1.421
T2	1.884	281	1901	5.396	2.247
T3	3.502	988	1165	4.151	1.724
T4	2.362	559	1032	5.791	2.321
T5	0.907	179	1116	2.774	1.318
T6	0.929	206	1091	5.127	2.100
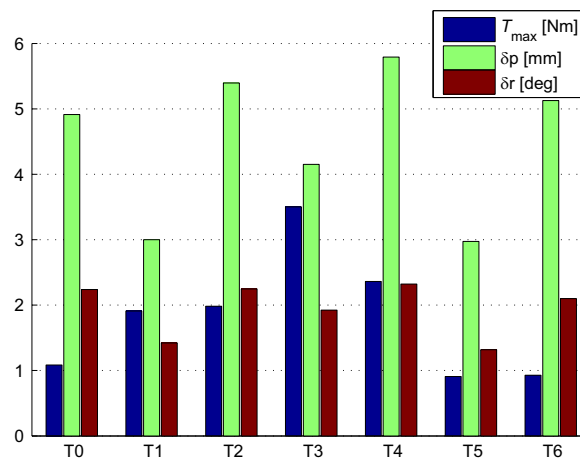
Fig. 13. Comparison of maximum actuator torques and deformations.

7. Conclusions

This paper addresses the architecture optimization problem of a parallel Schönflies-motion robot, for which the performances should be optimized with respect to dedicated PnP trajectories in a predefined workspace. Parametric models of the transmission quality, elasto-statics and dynamics were developed and further used in the optimal design procedure. The dimensional inhomogeneity in the manipulability evaluation due to the kinematic Jacobian matrix was accommodated by means of the concept of virtual power coefficient, namely, the motion/force transmission, from which a new transmission index was defined by the product of the input and output transmission indices for a better indication of the manipulability.

The main contribution is the formulation of a systematic procedure for task-oriented optimal design. The robot's architectural parameters were optimized within a predefined workspace based on a multi-objective optimization approach, where the performances were evaluated along the pick-and-place trajectory towards applications.

It is also found from the design optimization that the length of the connecting bar in the parallelogram has influence to the robot accuracy, namely, the longer the length, the higher the accuracy. This implies that the short bar in the parallelogram linkage should keep a reasonable length to ensure a high positioning accuracy.
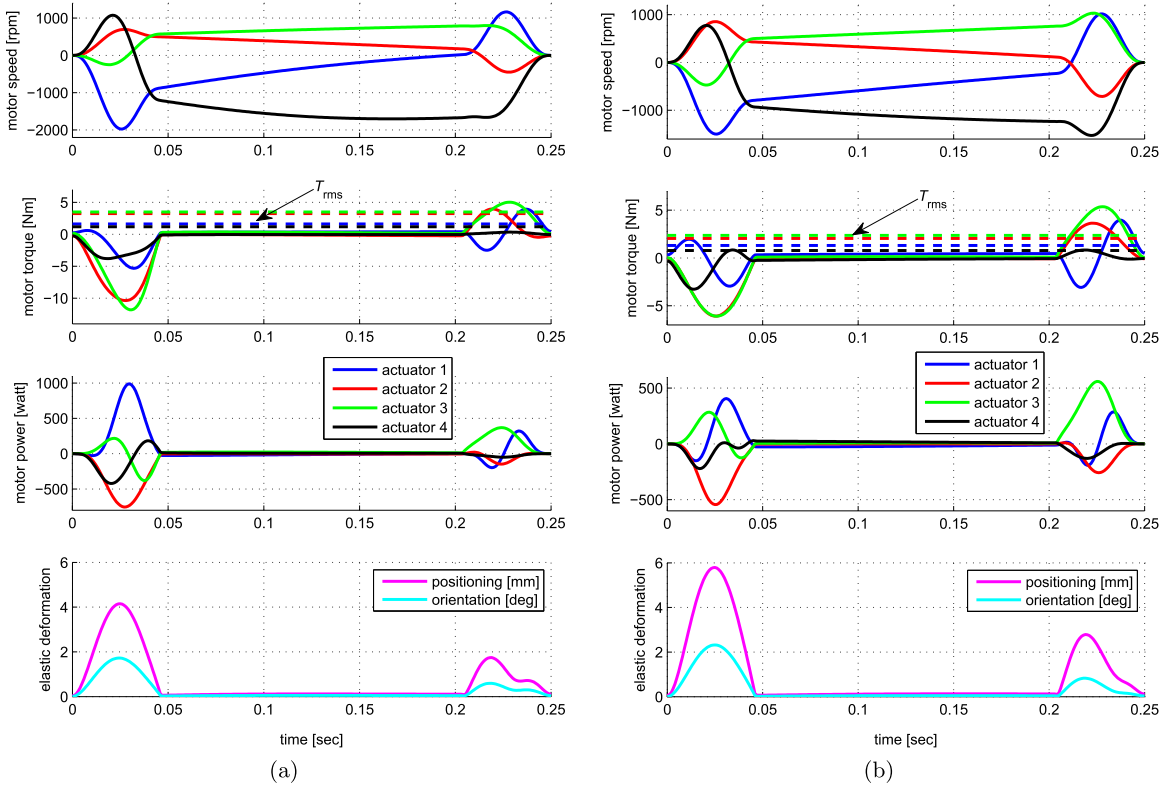
Fig. 14. The motor behaviors and the elastic deformations along the trajectories T3 (a) and T4 (b) of design ID-III.
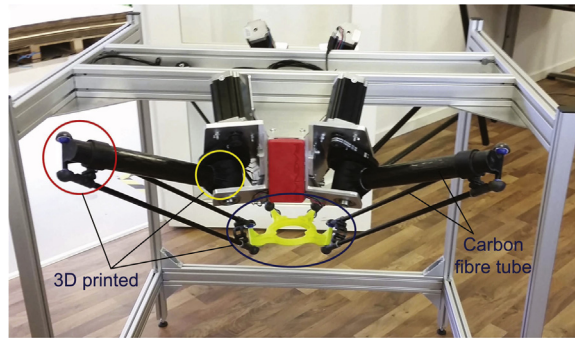

Fig. 15. A prototype of Ragnar robot with 3D-printed components.

The optimization was done for the Ragnar robot. As a matter of fact, the Ragnar can be considered as a more generalized parallel pick-and-place robot with four limbs. The Ragnar robot becomes a Quattro architecture based robot, i.e., X4 robot, if $a_x = a_y$, $\alpha = 45°$ and $\beta = 90°$. From this point of view, the method in this work is of general purpose and can be applicable to other parallel robots.

Acknowledgment

Appendix A. Degree-of-freedom of the robot

The degree-of-freedom of the manipulator under study is derived by the Group Theory. The robot is composed of four RRΠRR typed limbs as shown in Fig. 16 and the bond $\mathcal{L}_i$ of the i th limb is the product of the following five bonds:
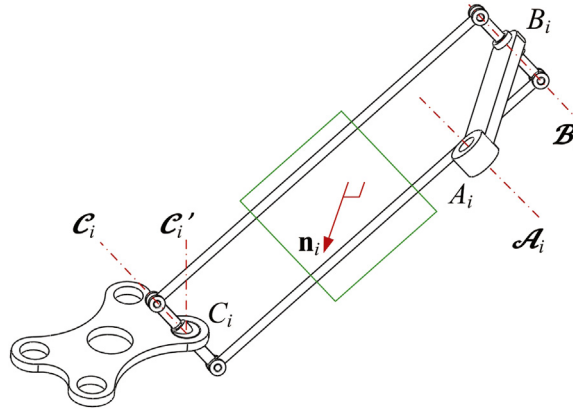
Fig. 16. The joints of the i th limb with rotational input.

- The rotation subgroup $\mathcal{R}(\mathcal{A}_i)$ of axis of rotation $\mathcal{A}_i$ passing through A_i and parallel to $\mathbf{e}_i$.
- The rotation subgroup $\mathcal{R}(\mathcal{B}_i)$ of axis of rotation $\mathcal{B}_i$ passing through B_i and parallel to $\mathcal{A}_i$.
- The translation subgroup $\mathcal{T}(\mathbf{n}_i)$ corresponding to the Π-joint lying in a plane normal to $\mathbf{n}_i$.
- The rotation subgroup $\mathcal{R}(C_i)$ of axis of rotation C_i passing through C_i and parallel to $\mathcal{B}_i$.
- The rotation subgroup $\mathcal{R}(C_{,i})$ of axis of rotation $C_{,i}$ passing through C_i and parallel to $\mathbf{k}$.

and $\mathbf{k}$ is the unit vector of z-axis. Thus, the kinematic bonds of the i th limb is

$$\mathcal{L}_i = \mathcal{R}(\mathcal{A}_i) \cdot \mathcal{R}(\mathcal{B}_i) \cdot \mathcal{T}(\mathbf{n}_i) \cdot \mathcal{R}(C_i) \cdot \mathcal{R}(C_{,i}) \tag{A.1}$$

where the product of the first four bonds leads to the Schönflies group, namely,

$$\mathcal{L}_i = \mathcal{X}(\mathbf{e}_i) \cdot \mathcal{R}(C_{,i}) \equiv \mathcal{X}(\mathbf{k}) \cdot \mathcal{R}(C_i) \tag{A.2}$$

Therefore, the intersection of the four limbs yields

$$\mathcal{L}_1 \cap \mathcal{L}_2 \cap \mathcal{L}_3 \cap \mathcal{L}_4 = \mathcal{X}(\mathbf{k}) \tag{A.3}$$

Henceforth, the intersection of all subgroups being a Schönflies subgroup $\mathcal{X}(\mathbf{k})$, the robot generates the Schönflies motion.

Appendix B. Stiffness matrix of the parallelogram

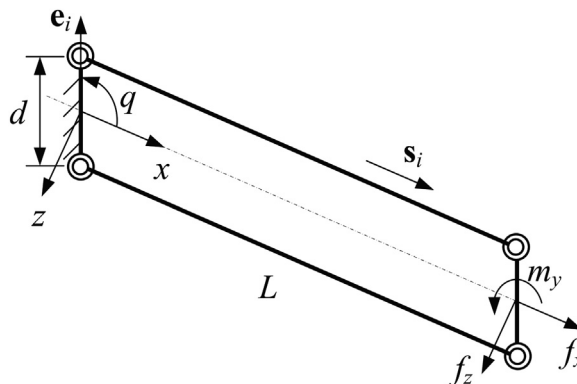The stiffness matrix of the parallelogram as shown in Fig. 17 is calculated as:

Fig. 17. The coordinate systems and force diagram of a parallelogram.

$$\mathbf{K}_\Pi = \begin{bmatrix} k_{11} + \dfrac{k_{55}d^2 S_q^2}{4} & 0 & \dfrac{k_{55}d^2 S_{2q}}{8} & 0 & 0 \\ 0 & \dfrac{k_{44}d^2 S_q^2}{4} & 0 & 0 & 0 \\ \dfrac{k_{55}d^2 S_{2q}}{8} & 0 & k_{33} + \dfrac{k_{55}d^2 C_q^2}{4} & 0 & k_{35} \\ 0 & 0 & 0 & k_{44} & 0 \\ 0 & 0 & k_{35} & 0 & k_{55} \end{bmatrix} \tag{B.1}$$

where $S_q = \sin q$, $C_q = \cos q$, $S_{2q} = \sin(2q)$, $q = \cos^{-1}(\mathbf{e}_i \cdot \mathbf{s}_i)$, and k_{ij} are expressed in Eq. (28).

References

[1] Adept Quattro Parallel Robots 〈http://www1.adept.com/main/ke/data/Archived/Quattro/sQuattro_UG.pdf.〉.
[2] F. Pierrot, C. Reynaud, A. Fournier, DELTA: a simple and efficient parallel robot, Robotica 8 (2) (1990) 105–109.
[3] S. Krut, V. Nabat, O. Company, F. Pierrot, A high-speed parallel robot for SCARA motions, in: IEEE International Conference on Robotics and Automation, 2004, pp. 4109–4115.
[4] F. Pierrot, V. Nabat, O. Company, S. Krut, P. Poignet, Optimal design of a 4-dof parallel manipulator: from academia to industry, IEEE Trans. Robot. 25 (2) (2009) 213–224.
[5] S.M. Kim, W. Kim, B.-J. Yi, Kinematic analysis and optimal design of a 3T1R type parallel mechanism, in: IEEE International Conference on Robotics and Automation, 2009, pp. 2199–2204.
[6] O. Altuzarra, B. Şandru, Ch. Pinto, V. Petuya, A symmetric parallel Schönflies-motion manipulator for pick-and-place operations, Robotica 29 (2011) 853–862.
[7] Penta Veloce 〈http://pentarobotics.com/products/#brochure.〉.
[8] F. Xie, X. Liu, Design and development of a high-speed and high-rotation robot with four identical arms and a single platform, ASME J. Mech. Robot. 7 (4) (2015) 041015.
[9] X. Kong, C.M. Gosselin, Type synthesis of 3T1R 4-dof parallel manipulators based on screw theory, IEEE Trans. Robot. Autom 20 (2) (2004) 181–190.
[10] J. Angeles, S. Caro, W. Khan, A. Morozov, Kinetostatic design of an innovative Schönflies-motion generator, Proc. Inst. Mech. Eng. Part C: J. Mech. Eng. Sci. 220 (7) (2006) 935–943.
[11] T. Harada, J. Angeles, Kinematics and singularity analysis of a CRRHHRRC parallel Schönflies motion generator, CSME Trans. 38 (2) (2014) 173–183.
[12] G. Wu, S. Bai, P. Hjørnet, Design analysis and dynamic modeling of a high-speed 3T1R pick-and-place parallel robot, in: S. Bai, M. Ceccarelli (Eds.), Mechanisms and Machine Science: Recent Advances in Mechanism Design for Robotics, vol. 33, 2015, pp. 285–295.
[13] J.S. Dai, D.G. Caldwell, Robotics and automation for packaging in the confectionery industry, Robot. Autom. Food Ind. (2012) 401–419.
[14] R.E. Stamper, L.-W. Tsai, G.C. Walsh, Optimization of a three DOF translational platform for well-conditioned workspace, in: IEEE International Conference on Robotics and Automation, 1997, pp. 3250–3255.
[15] J.-P. Merlet, Jacobian, manipulability, condition number, and accuracy of parallel robots, ASME J. Mech. Des. 128 (1) (2006) 199–206.
[16] O. Altuzarra, A. Hernandez, O. Salgado, J. Angeles, Multiobjective optimum design of a symmetric parallel Schönflies-motion generator, ASME J. Mech. Des. 131 (3) (2009) 031002.
[17] A. Taghvaeipour, J. Angeles, L. Lessard, Optimum structural design of a two-limb Schönflies motion generator, Mech. Mach. Theory 80 (2014) 125–141.
[18] A. Cammarata, R. Sinatra, Elastodynamic optimization of a 3T1R parallel manipulator, Mech. Mach. Theory 73 (2014) 184–196.
[19] D. Corbel, M. Gouttefarde, O. Company, F. Pierrot, Actuation redundancy as a way to improve the acceleration capabilities of 3T and 3T1R pick-and-place parallel manipulators, ASME J. Mech. Robot. 2 (4) (2010) 041002.
[20] S. Liu, T. Huang, J. Mei, X. Zhao, P. Wang, D.G. Chetwynd, Optimal design of a 4-DOF SCARA type parallel robot using dynamic performance indices and angular constraints, ASME J. Mech. Robot. 4 (3) (2012) 031005.
[21] D. Chablat, S. Caro, R. Ur-Rehman, P. Wenger, Comparison of planar parallel manipulator architectures based on a multi-objective design optimization approach, in: ASME 2010 International Design Engineering Technical Conferences (IDETC/CIE), 2010, pp. 861–870.
[22] A. Hernández, O. Altuzarra, O. Salgado, C. Pinto, V. Petuya, Designing parallel manipulators: from specifications to a real prototype, Ind. Robot 39 (5) (2012) 500–512.
[23] D. Chablat, P. Wenger, Architecture optimization of a 3-DOF translational parallel mechanism for machining applications, the Orthoglide, IEEE Trans. Robot. Autom. 19 (3) (2003) 403–410.
[24] G. Wu, S. Bai, P. Hjørnet, Parametric optimal design of a parallel Schönflies-motion robot under pick-and-place trajectory constraints. in: IEEE/RSJ International Conference on Intelligent Robots and Systems, Hamburg, Germany, 2015, pp. 3158–3163.
[25] C. Chen, J. Angeles, Generalized transmission index and transmission quality for spatial linkages, Mech. Mach. Theory 42 (9) (2007) 1225–1237.
[26] R. Hartenberg, J. Denavit, Kinematic Synthesis of Linkages, McGraw-Hill, New York, 1964.
[27] J.S. Wang, X.J. Liu, C. Wu, Optimal design of a new spatial 3-dof parallel robot with respect to a frame-free index, Sci. China Ser. E 52 (4) (2009) 986–999.
[28] J. Wang, C. Wu, X. Liu, Performance evaluation of parallel manipulators: Motion/force transmissibility and its index, Mech. Mach. Theory 45 (10) (2010) 1462–1476.
[29] G. Wu, S. Caro, J. Wang, Design and transmission analysis of an asymmetrical spherical parallel manipulator, Mech. Mach. Theory 94 (2015) 119–131.
[30] C. Gosselin, Stiffness mapping for parallel manipulators, IEEE Trans. Robot. Autom. 6 (3) (1990) 377–382.
[31] S.-F. Chen, I. Kao, Conservative congruence transformation for joint and cartesian stiffness matrices of robotic hands and fingers, Int. J. Robot. Res. 19 (2000) 835–847.
[32] G. Alici, B. Shirinzadeh, Enhanced stiffness modeling, identification and characterization for robot manipulators, IEEE Trans. Robot. 21(4) (2005) 554–564.
[33] F. Majou, C. Gosselin, P. Wenger, D. Chablat, Parametric stiffness analysis of the Orthoglide, Mech. Mach. Theory 42 (3) (2007) 296–311.
[34] A. Pashkevich, D. Chablat, P. Wenger, Stiffness analysis of overconstrained parallel manipulators, Mech. Mach. Theory 44 (5) (2009) 966–982.
[35] G. Wu, S. Bai, P. Hjørnet, On the stiffness of three/four degree-of-freedom parallel pick-and-place robots with four identical limbs, in: IEEE International Conference on Robotics and Automation, 11–16 May 2016, Stockholm, Sweden, 2016, pp. 861–866.
[36] G. Wu, S. Bai, J. Kepler, Mobile platform center shift in spherical parallel manipulators with flexible limbs, Mech. Mach. Theory 75 (2014) 12–26.
[37] J.G. De Jalon, E. Bayo, Kinematic and Dynamic Simulation of Multibody Systems: The Real-time Challenge, Springer Science & Business Media, New York, 2012.
[38] E. Abbena, S. Salamon, A. Gray, Modern Differential Geometry of Curves and Surfaces With Mathematica, CRC Press, London, 2006.
[39] K. Deb, A. Pratap, S. Agarwal, T. Meyarivan, A fast and elitist multiobjective genetic algorithm: NSGA-II, IEEE Trans. Evol. Comput. 6 (2) (2002) 182–197.